Figure S1: Spatial distribution of differences between shortwave dust direct radiative effect (DRE) at the top of the atmosphere (TOA, dust DRE in the following supplementary figures refers to the value at the TOA by default) in CAM5 after and before correction using C1999 with high-bound hematite in the clay-sized category (a) and high-bound dust AOD (b).

a) HiHemClay correction: +0.02 W m^{-2}

b) HigherDOD correction: +0.05 W m^{-2}
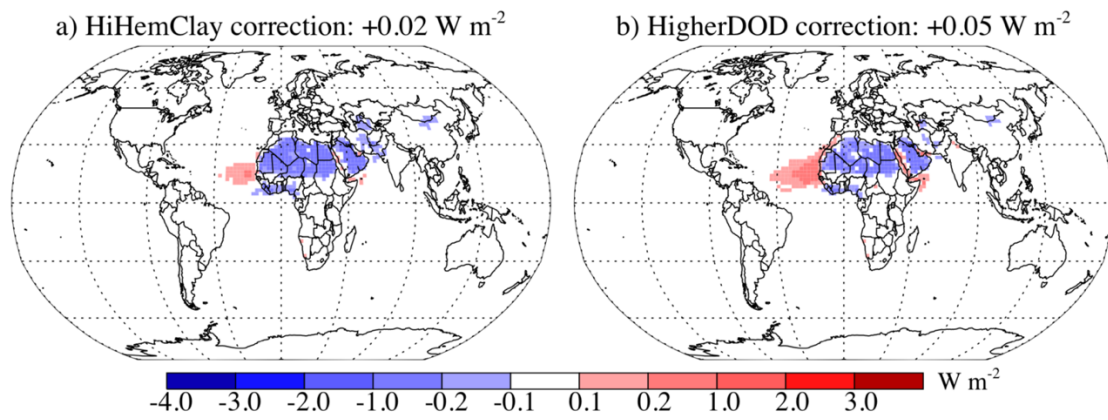
Figure S2: Soil distribution of illite in the clay-sized category (a, Ill_clay), kaolinite in the clay-sized category (b, Kao_clay), smectite in the clay-sized category (c, Mon_clay), hematite in the clay-sized category (d, Hem_clay), calcite in the clay-sized category (e, Cal_clay), quartz in the clay-sized category (f, Qua_clay) and silt-sized category (l, Qua_silt) , feldspar in the clay-sized category (g, Fel_clay) and silt-size category (m, Fel_silt), goethite in the clay-sized category (h, Goe_clay) and silt-sized category (h, Goe_silt) and gypsum in the silt-sized category (I, Gyp_silt). Choloride, mica, vermiculite in the silt-sized category are merged into one, which is represented by kao_silt.
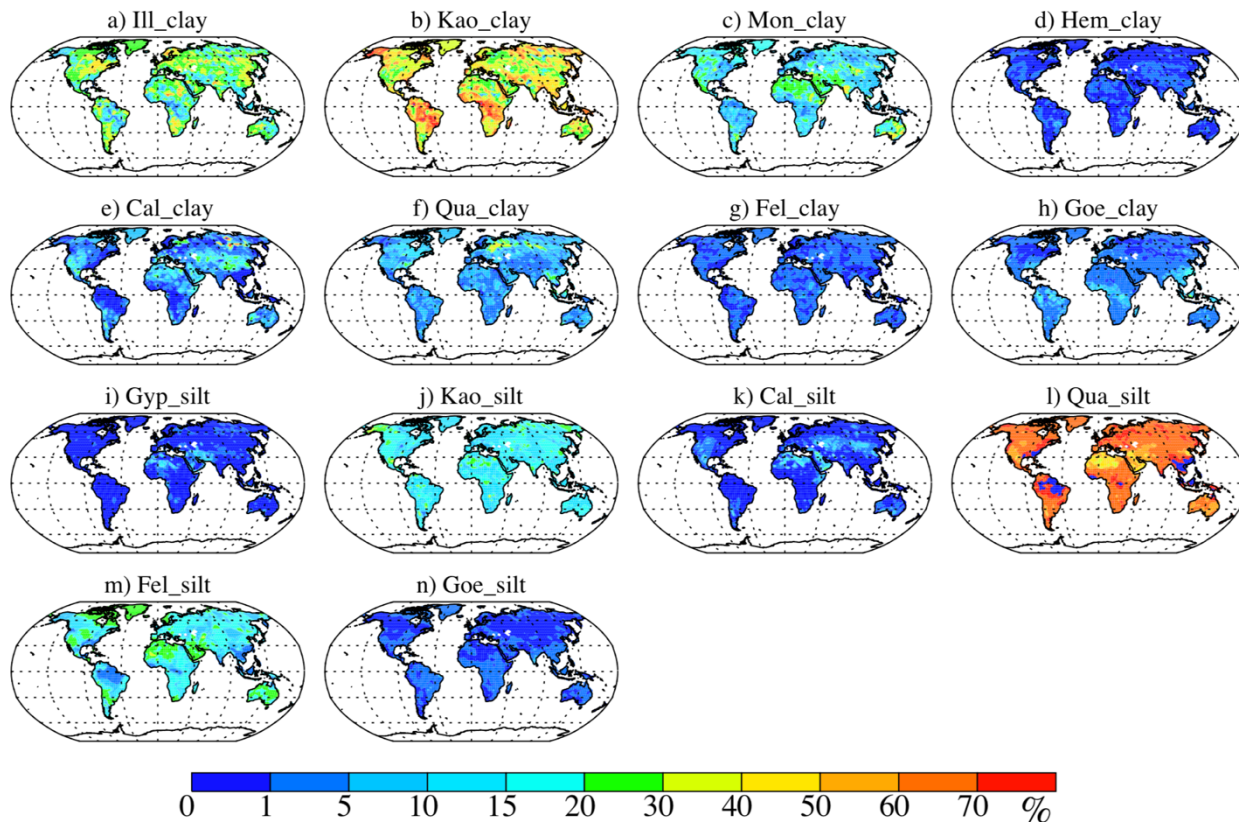
Figure S3: Difference between soil abundance of minerals in the clay- and/or silt-sized categories in J2014 and C1999. There is no hematite in the silt-sized category in J2014, and no kaolinite and goethite in the silt-sized category in C1999. Shown minerals are illite in the clay-sized category (a, Ill_clay), kaolinite in the clay-sized category (b, Kao_clay), smectite in the clay-sized category (c, Mon_clay), hematite in the clay-sized category (d, Hem_clay), goethite in the clay-sized category (Goe_clay), calcite in the clay-sized category (e, Cal_clay), quartz in the clay-sized category (f, Qua_clay) and silt-sized category (i, Qua_silt), gypsum in the silt-sized category (g, Gyp_silt), calcite in the clay-sized category (h, Cal_silt), feldspar in the silt-sized category (j, Fel_silt), and goethite in the silt-sized category (k, Goe_silt). No feldspar is present in the clay-sized category in C1999.
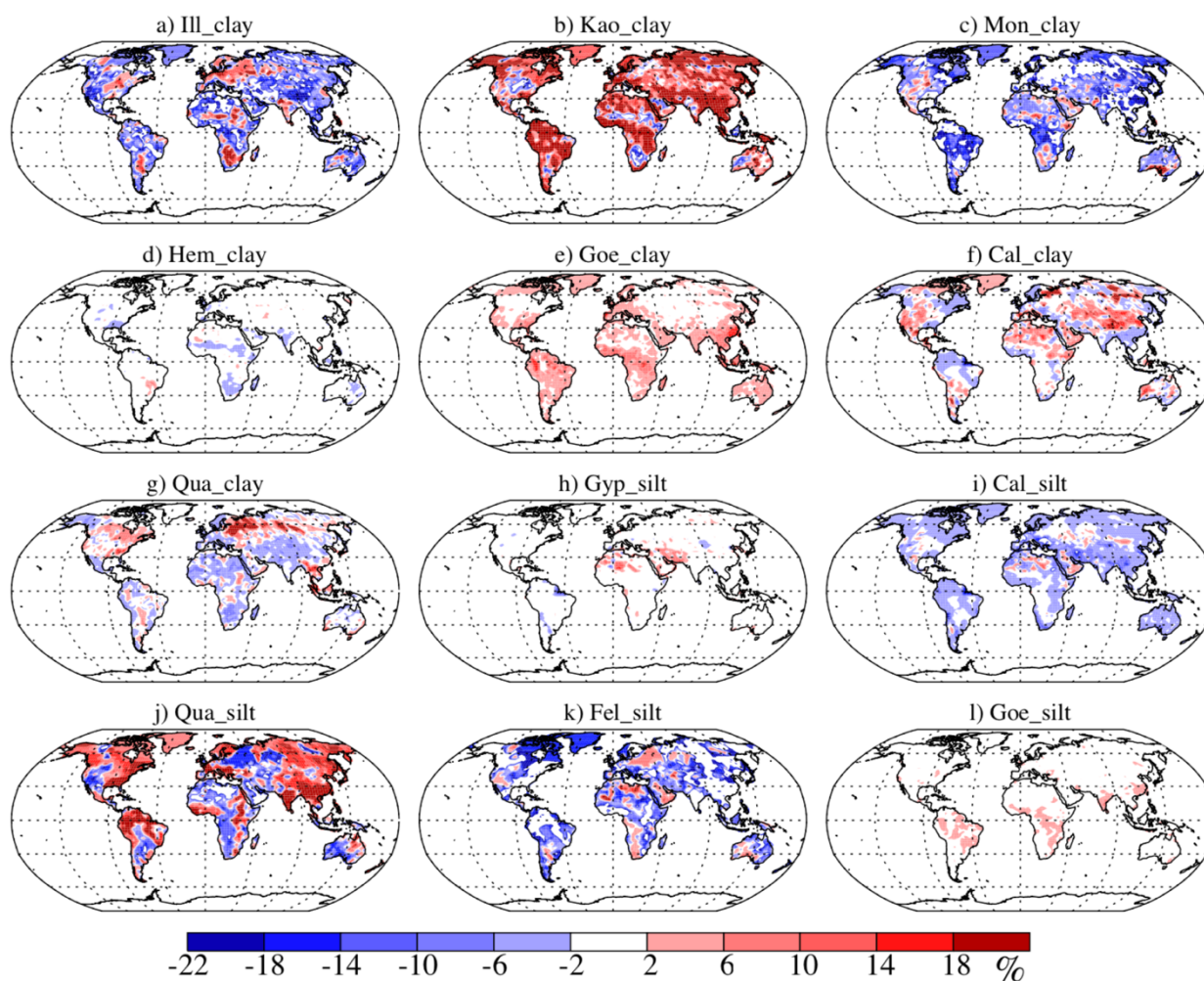
Figure S4: The root mean square errors (RMSE) for the shortwave DRE prediction based on the least square regression in CAM5 by using the slope obtained with simulated hematite aerosol mass (a) and dust AOD (c), and shortwave DRE in CAM5. Also shown is the global mean of the predicted shortwave DRE against the actual value in CAM5 with high-bound hematite in the clay-sized category (b) and dust AOD in the baseline simulation (d).
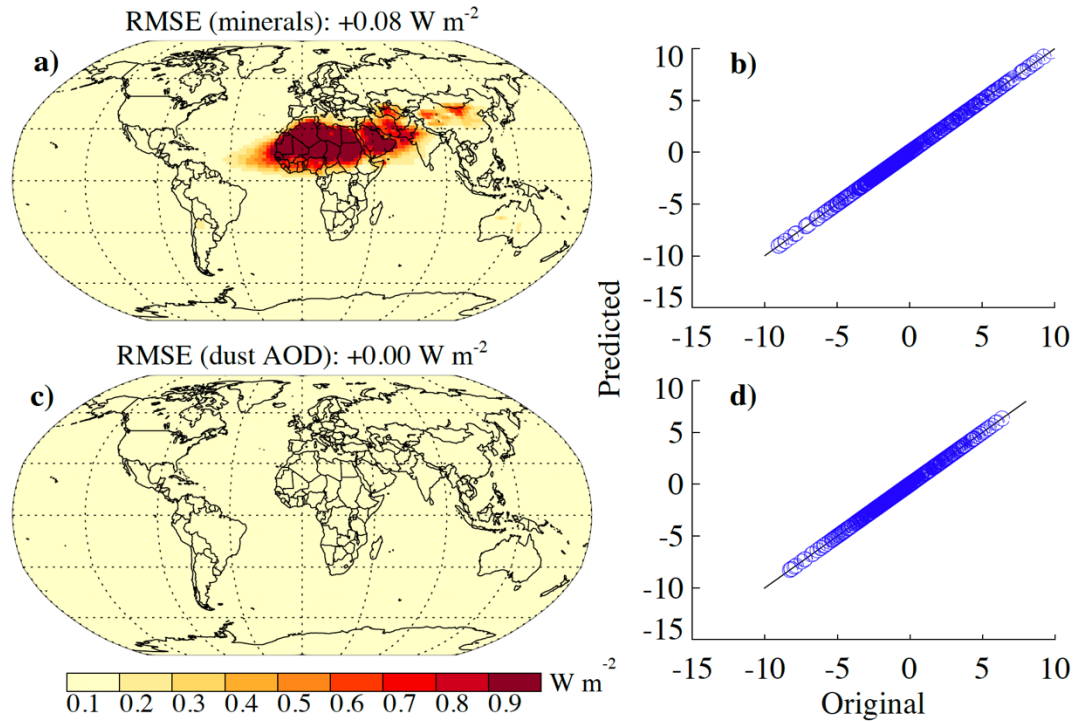
Figure S5: The root mean square errors (RMSE) for the shortwave DRE prediction based on the least square regression in CAM6 by using the slope obtained with simulated hematite aerosol mass (a) and dust AOD (c), and shortwave DRE in CAM5. Also shown is the global mean of the predicted shortwave DRE against the actual value in CAM5 with high-bound hematite in the clay-sized category (b) and dust AOD in the baseline simulation (d).
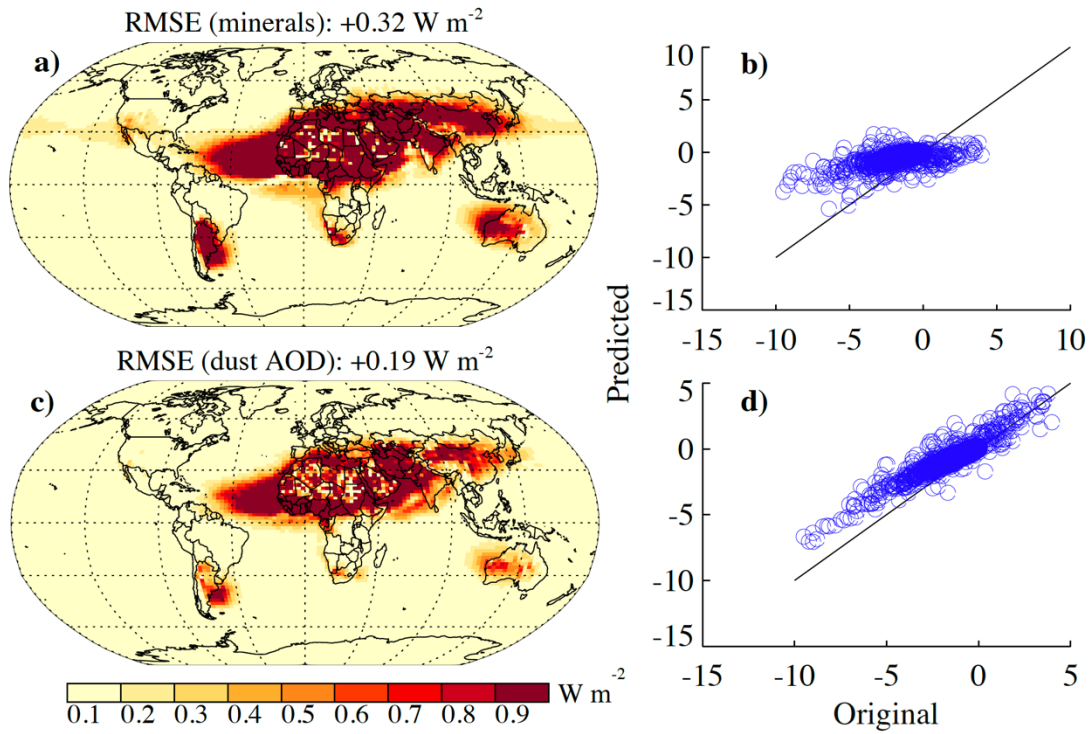
Figure S6: Difference between predicted shortwave DRE based on simulated hematite aerosol mass with high-bound hematite in the clay-sized category in CAM5 with C1999 and CAM5-baseline value (panel a), and between predicted shortwave DRE based on dust AOD in the baseline and the baseline value (panel b).
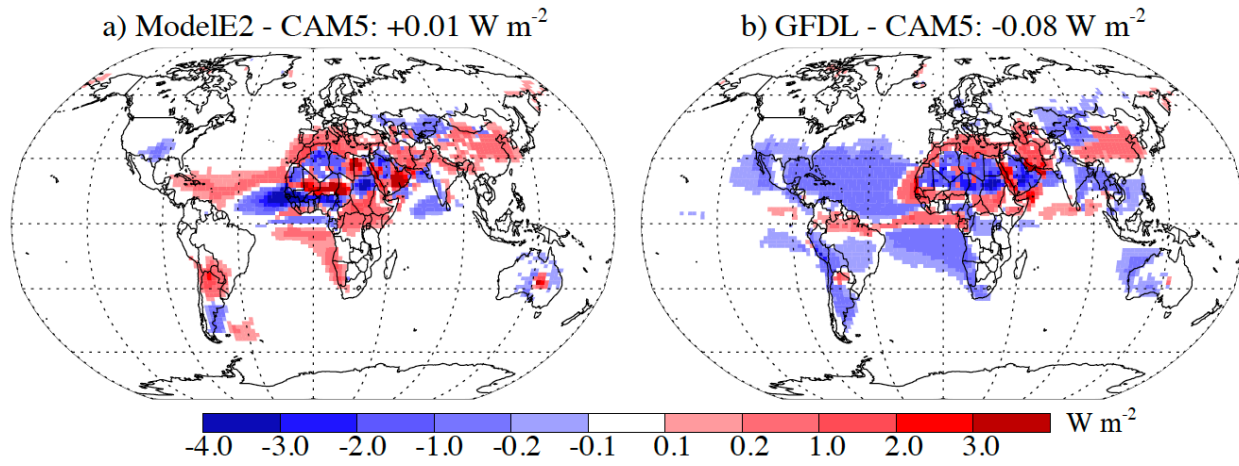
Figure S7: The root mean square errors (RMSE) of the regression-based shortwave DRE prediction obtained by applying the relationship between shortwave DRE and dust AOD in the CAM5 baseline simulation to CAM5 with the high-bound dust AOD (a) and to MONARCH (c). Also shown is the global mean of the predicted shortwave DRE against the actual value in CAM5 with the high-bound dust AOD (b) and MONARCH (d).
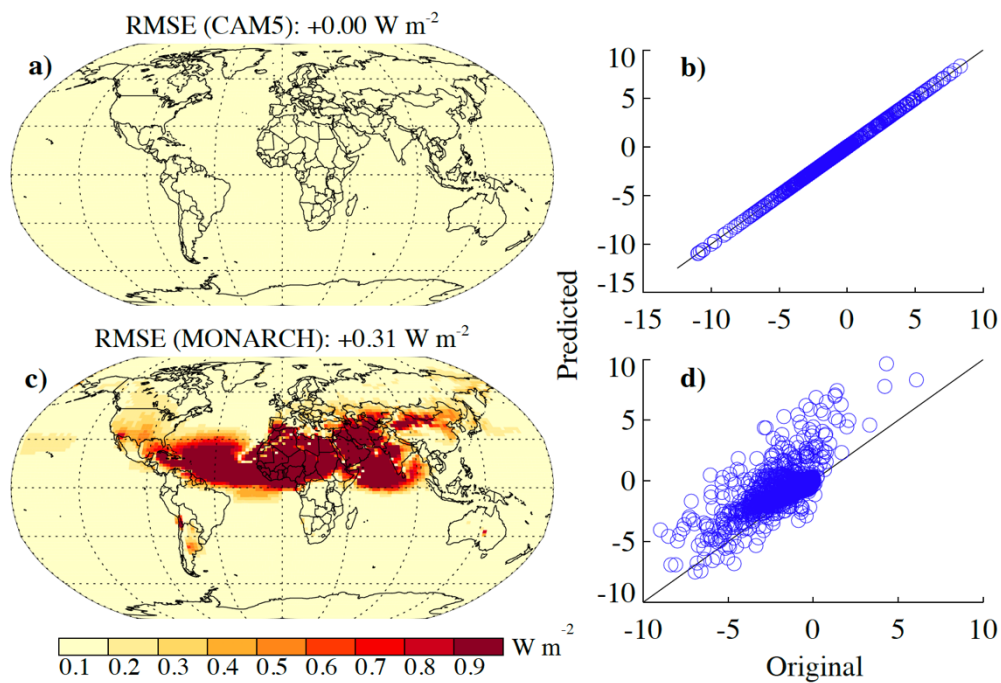
Figure S8: Relative change (in percentage) of simulated mass fraction for eight minerals in CAM5 with C1999 from base to high bound of their soil distribution. Relative change is defined as the (high bound – base)/base×100. Ill.-illite, Kao.-kaolinite, Mon.-montmorillonite, Qua.-quartz, Cal.-calcite, hem.-hematite, Fel.-feldspar, gyp.-gypsum.
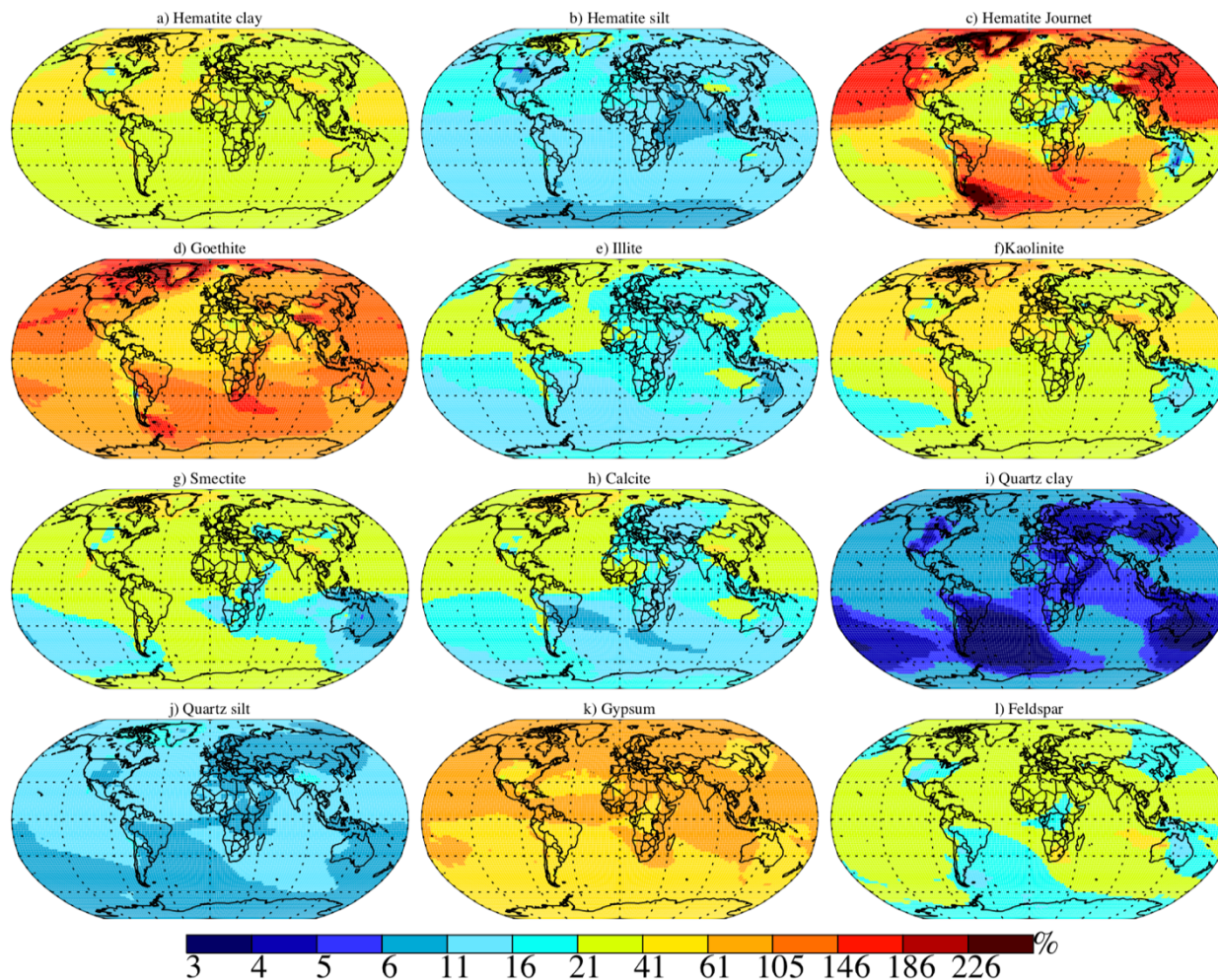
Figure S9: Spatial distributions of annually column mineral simulated (a,c,e,g,I,k,m,o) and the coefficient of variation (CV) (b,d,f,h,j,l,n,p), calculated as ratio of the standard deviation to mean for eight minerals in CAM6 with C1999 and CAM5 with C1999 and J2014. For each mineral, we calculate the sum of all three modes in the model. Ill.-illite, Kao.-kaolinite, Mon.-montmorillonite, Qua.-quartz, Cal.-calcite, hem.-hematite, Fel.-feldspar, gyp.-gypsum. Mean mass fractions for hematite and gypsum were scaled by 10.
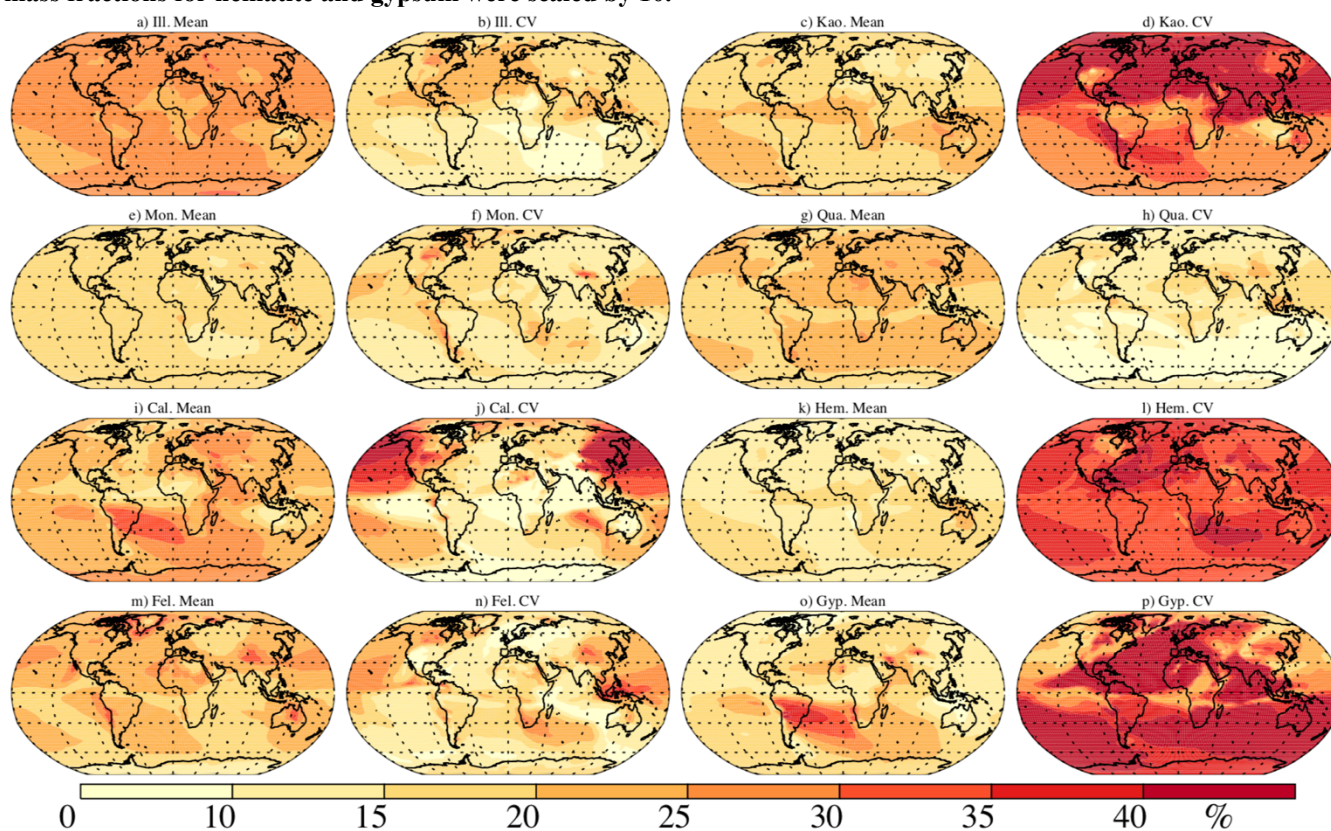
Figure S10: Distribution of simulated mean and coefficient of variation (CV) for hematite and goethite in C1999 (a and c) and both atlases (b and d) in CAM5, CAM6 (with C1999), and ModelE2 (with C1999). All cases in CAM5 with C1999 on perturbed hematite are included in the calculation. For simulations with J2014, goethite is implemented into the model as a separate tracer from hematite. In this figure, goethite is added to hematite to get the total mass fraction of iron oxides. CV is calculated as the ratio of the standard deviation of simulated iron oxides to their mean. Column mineral fractions from CAM6 and ModelE2 are regridded onto CAM5 grids for calculations.

a) Claquin: hem (mean)

b) Journet: hem & goe (mean)

c) Claquin: hem (CV)

d) Journet: hem & goe (CV)
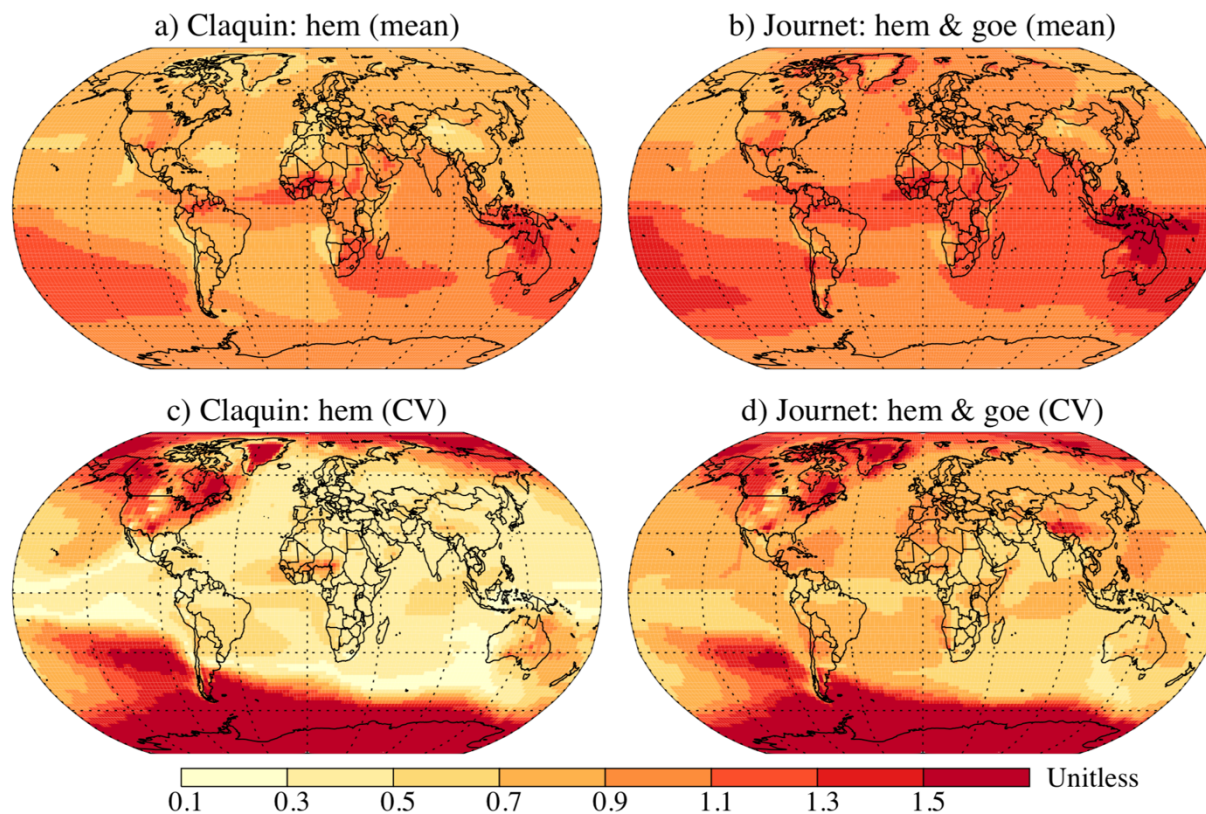
Figure S11: Distribution of simulated mean and coefficient of variation (CV) for hematite and goethite in C1999 (a and c) and both maps (b and d) soil datasets in CAM5. All cases in CAM5 with C1999 on perturbed hematite are included in the calculation. For simulations with J2014, goethite is implemented into the model as a separate tracer from hematite, but here it is added to hematite to get the total mass fraction of iron oxides. CV is calculated as the ratio of the standard deviation of simulated iron oxides to their mean.
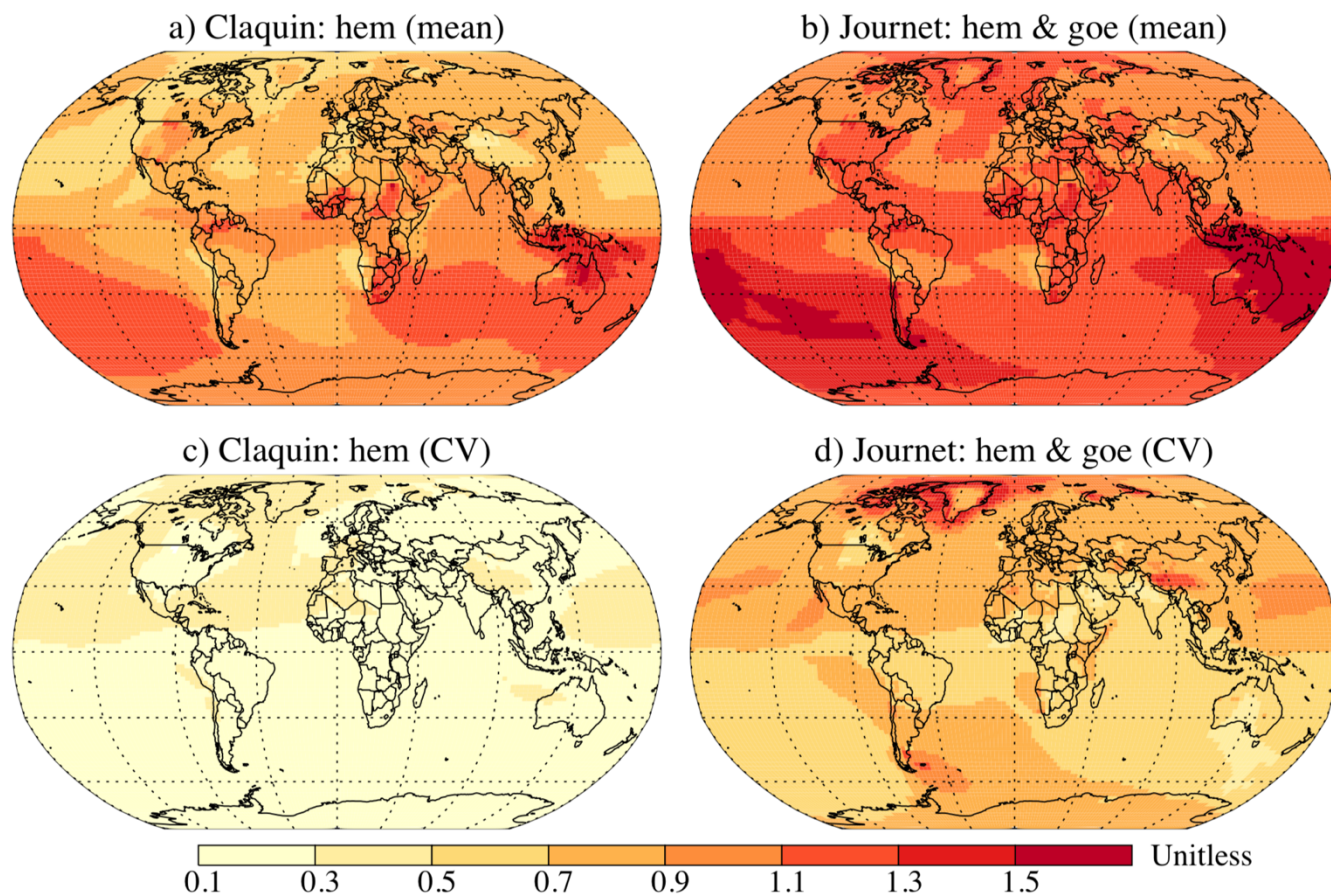
Figure S12: Distribution of simulated coefficient of variation (CV) for hematite in C1999 in CAM5 versus CAM6 (a), and CAM5 versus ModelE2 (b). Only the base case in models with C1999 are included in the calculation. CV is calculated as the ratio of the standard deviation of simulated iron oxides to their mean.
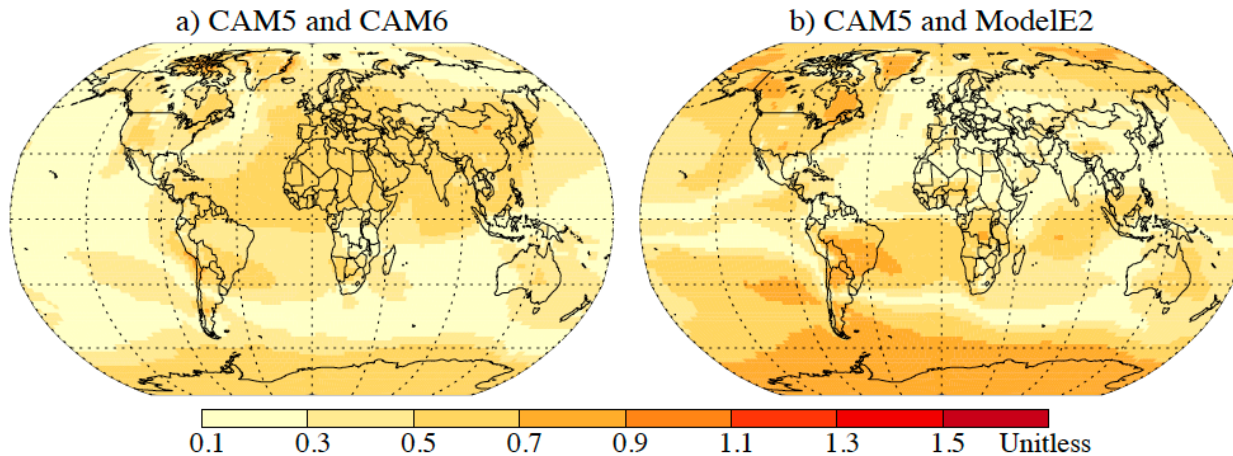
Figure S13: Deviation of shortwave DRE for different cases from the baseline simulation in CAM5 with C1999. Hi(Lw)HemClay(Silt)-high (low) bound of hematite in the clay-sized (silt-sized) category; Hi(Lw)IllClay-high (low) bound of illite in the clay-sized category; Hi(Lw)SmeClay-high (low) bound of smectite in the clay-sized category; HiKaoClay-high bound of kaolinite in the clay-sized category; Hi(Lw)FelSilt-high (low) bound of feldspar in the silt-sized category; Hi(Lw)QuaClay(Silt)-high (low) bound of quartz in the clay-sized (silt-sized) category; HiCalClay-high bound of calcite in the clay-sized category; HiGypSilt-high bound of gypsum in the silt-sized category; higher(lower) DOD-high (low) bound of dust AOD; higher(lower)IM-high (low) bound of imaginary complex refractive index.
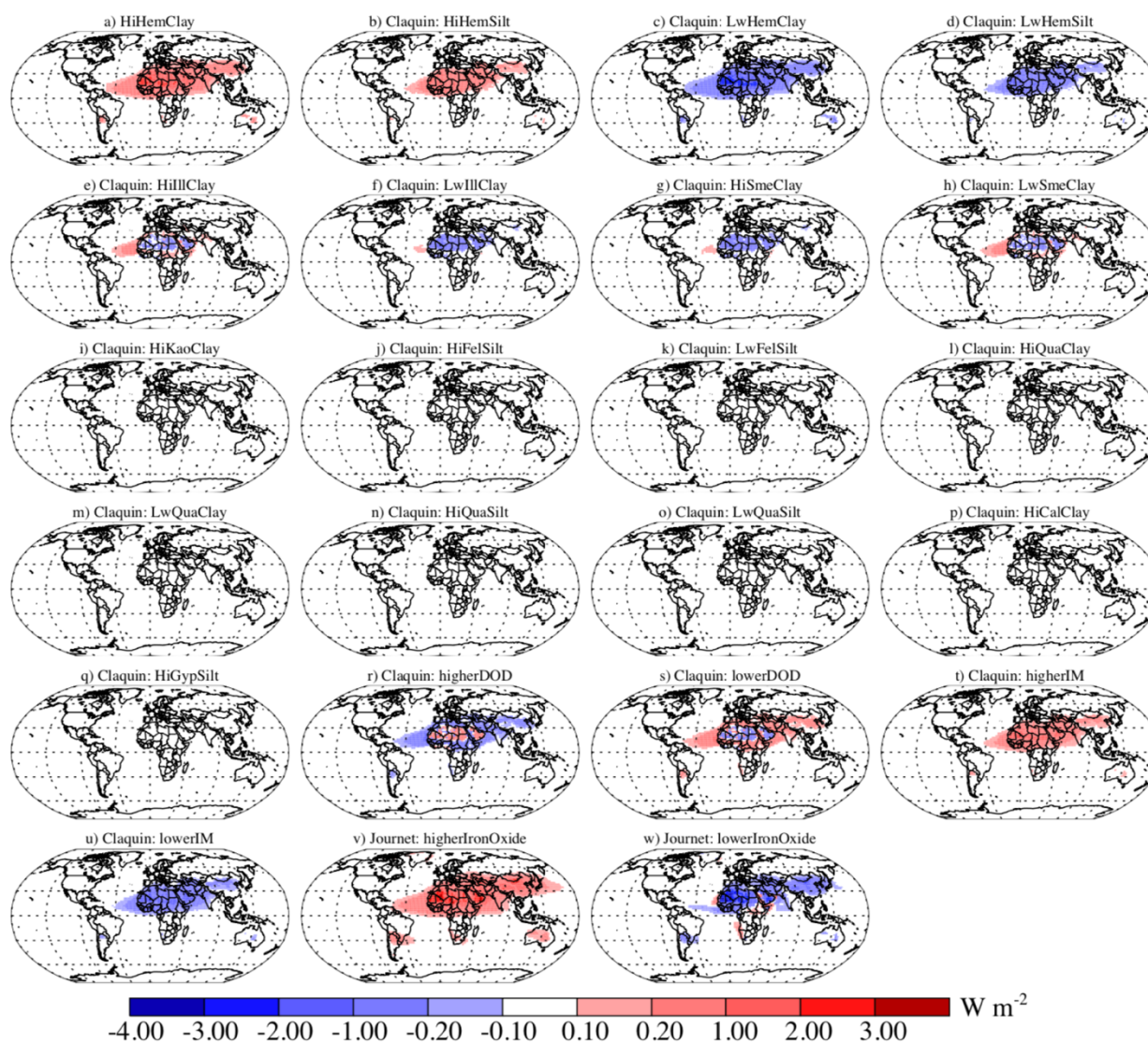
Figure S14: Shortwave dust DRE and its sensitivity to hematite (Hem) in clay- and silt-sized categories, smectite (Sme), and illite (Ill) in CAM4 with C1999. Bars: values associated with higher (in color) and lower bounds (dash with opposite signs to real values) of minerals. Black horizonal line in (a) denotes shortwave DRE in the baseline simulation.
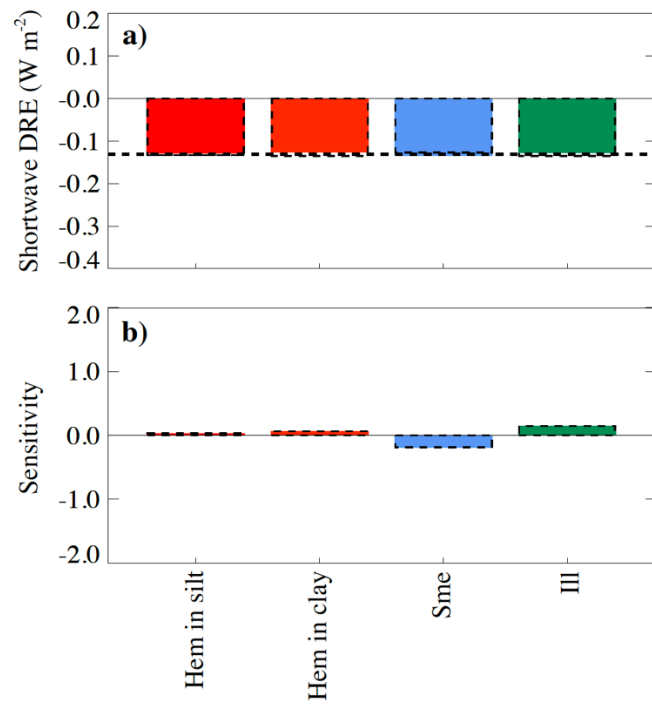
Figure S15: Isolated regions where changes of the shortwave DRE due to uncertainty in iron oxides including C1999 (a), and both C1999 and J2014 (b) significantly exceed the interannual variability of DRE at different confidence levels as indicated by the labels in percentage in CAM5.

a) Claquin

b) Claquin and Journet
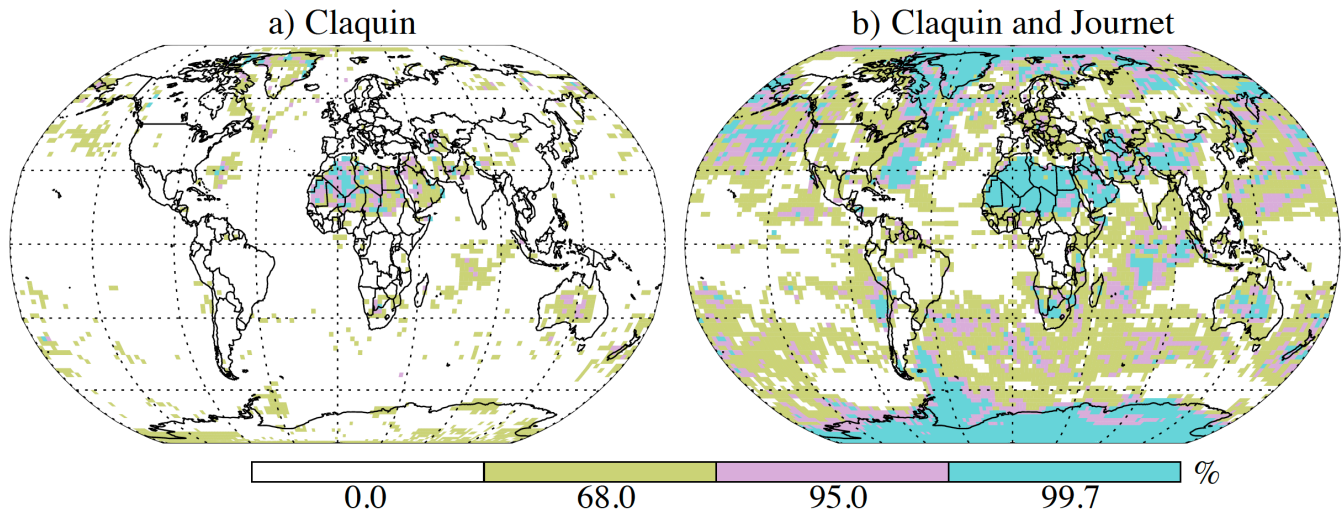
Figure S16: Spatial distribution of differences between the shortwave DRE in ModelE2 (regression) (a), and MONARCH (simulation) (b), and in the CAM5 baseline. Numbers represent global averages.

a) ModelE2 - CAM5: +0.09 W m^{-2} b) MONARCH - CAM5: -0.19 W m^{-2}
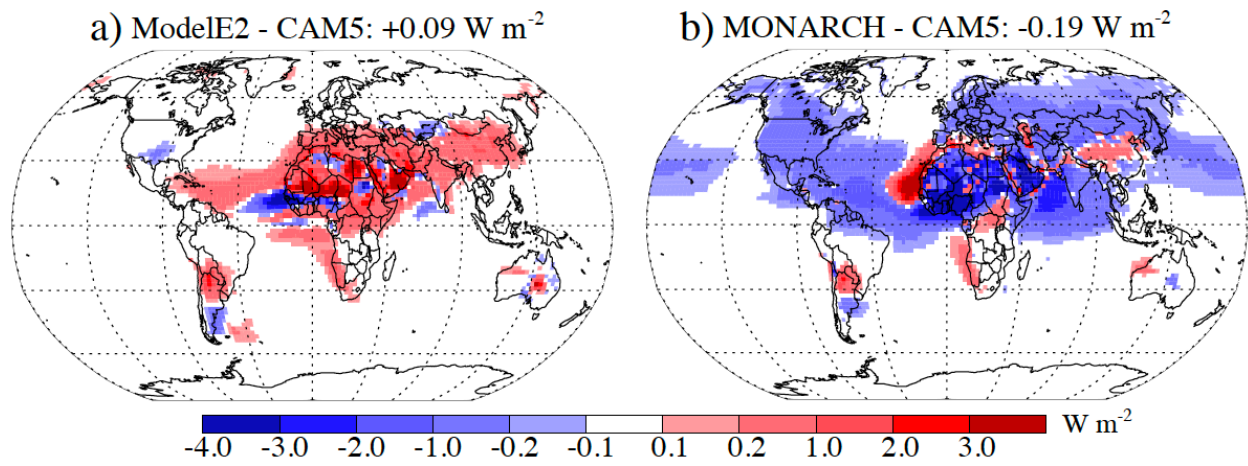
Figure S17: Spatial distribution of differences between the hematite aerosol mass (unit: 10^3 kg) simulated by ModelE2 and CAM5 with high-bound hematite in the clay-sized category.
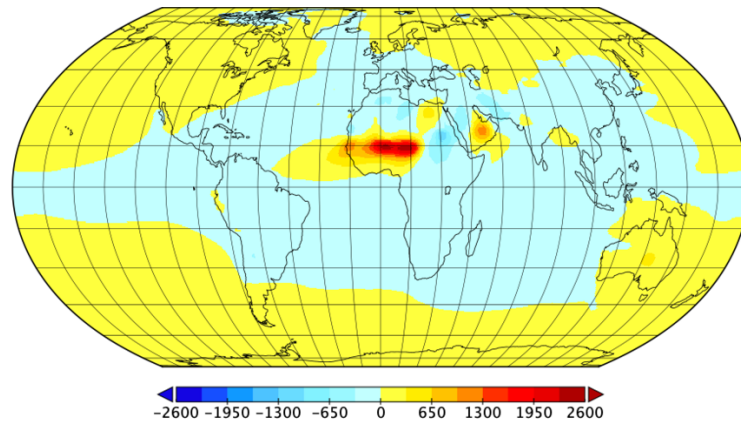
Figure S18: Distribution of upper-branch uncertainty in longwave DRE due to uncertainty in the soil abundance of feldspar and quartz. Values are obtained by taking the difference between the longwave DRE in CAM5 with the low-bound feldspar and quartz, and with the baseline. Panel a) for feldspar, b) and c) for quartz in the clay- and silt-sized categories, respectively, d) the sum of b) and c).

a) Fel: +0.0003 W m^{-2}

b) Qua(Clay): -0.0002 W m^{-2}

c) Qua(Silt): -0.0003 W m^{-2}

d) Qua(Clay+Silt): -0.0005 W m^{-2}

W m^{-2}

-0.022 -0.018 -0.014 -0.010 -0.006 -0.002 0.002 0.006 0.010 0.014 0.018
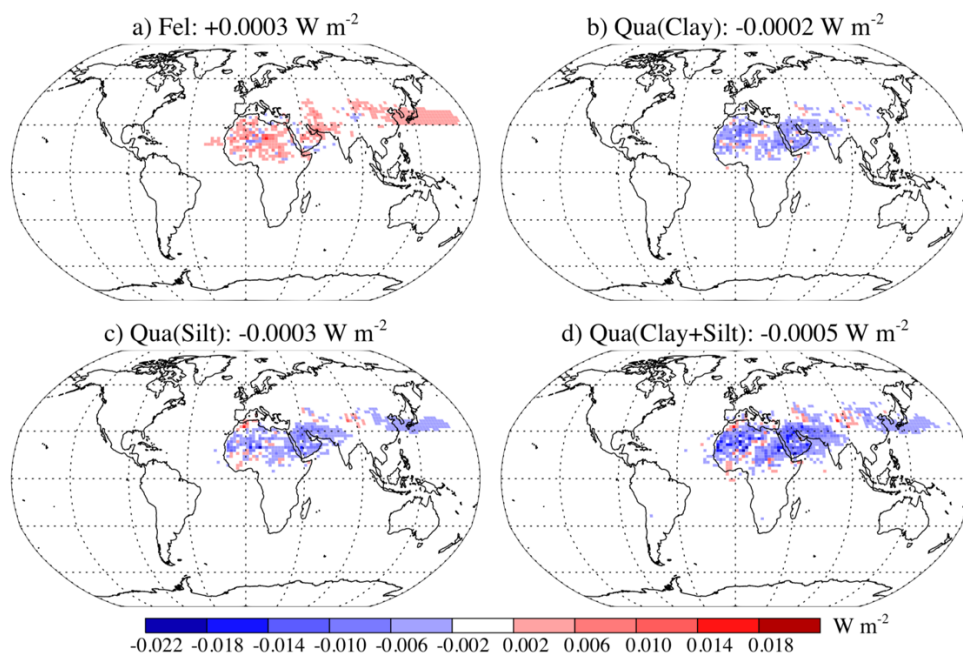
Figure S19: Imaginary complex refractive indices for minerals. Data source: Scanza et al., (2015). Shading areas represent water vapor absorption windows. Red arrows on the top of the plot show bands where quartz has stronger absorption than most other minerals, while blue arrows show bands where quartz has weaker absorption than most other minerals.
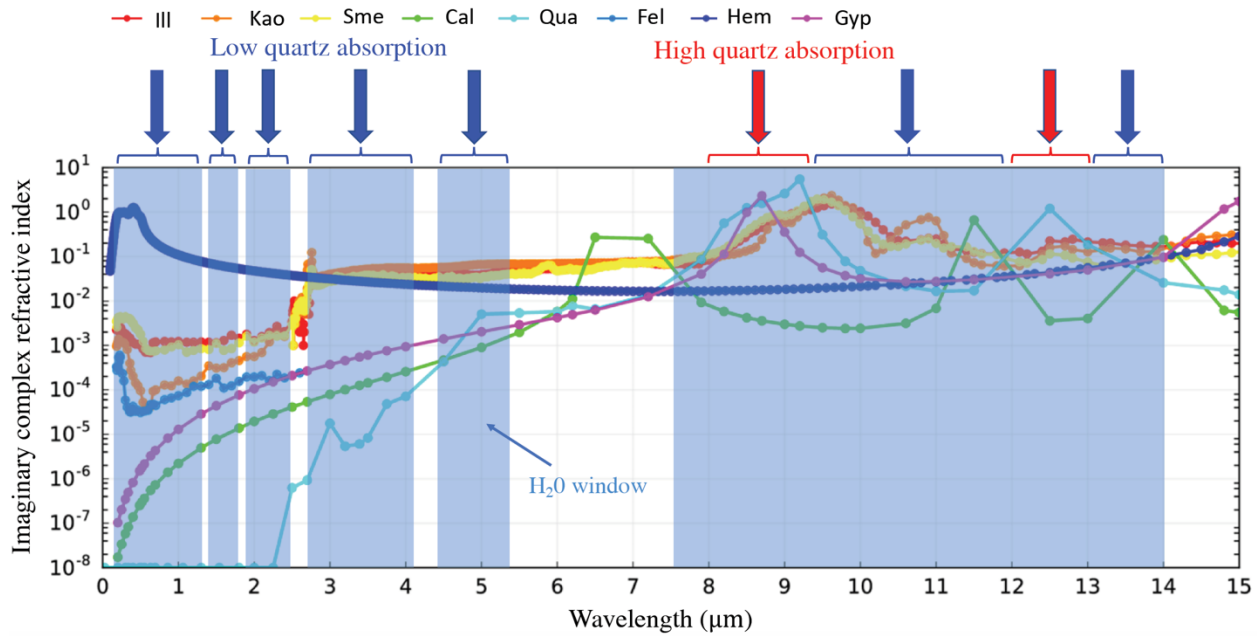
Figure S20: Imaginary complex refractive indices for minerals at longwave (near infrared and longwave) bands used in CAM. Data source: Scanza et al., (2015). The longwave band numbers are shown in Table S2. The near infrared band information is not shown.
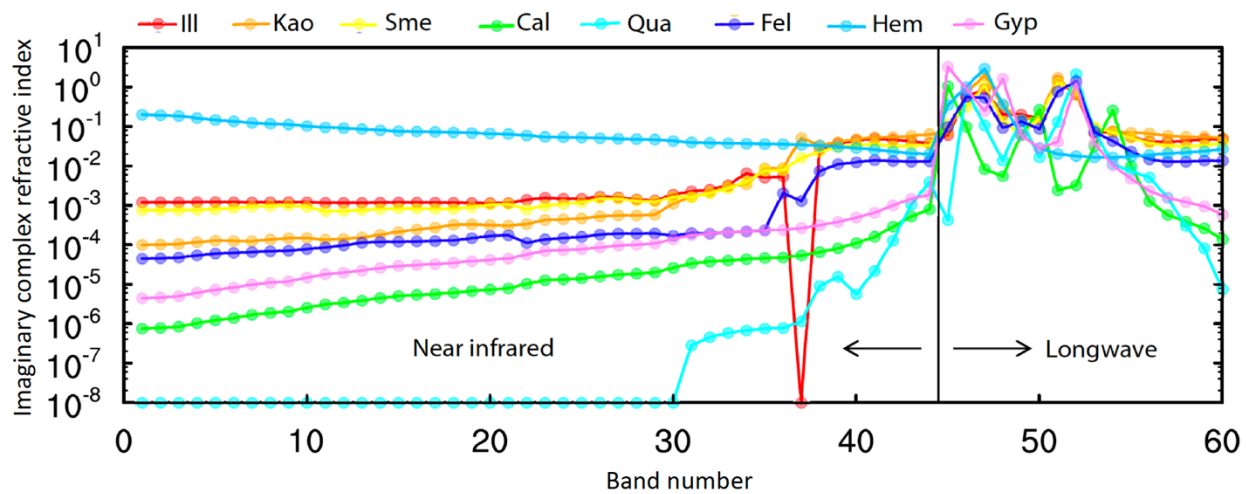
Figure S21: Upper branch of uncertainty in longwave DRE W m^{-2} with the global mean indicated in the title in CAM5 (a), and in CAM5 and MONARCH (b) including both C1999 and J2014 but neglecting dust scattering. Inlet numbers represent the global mean lower branch of longwave DRE uncertainty.
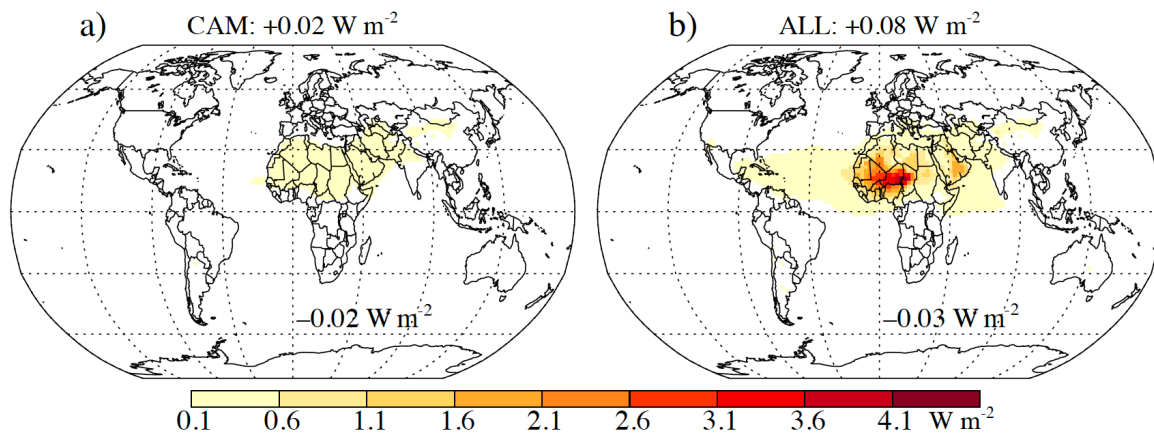
Table S1: Domain of the sub regions considered in Section 3.2.2.3

Region	Longitude range	Latitude Range
North Africa	20°W-35°E	5°N-40°N
Middle East	25°E-60°E	12°N-41°N
Central Asia	60°E-100°E	5°N-30°N
North East Asia	90°E-140°E	30°N-50°N
Australia	110°E-155°E	45°S-10°S

Table S2: Longwave band information in CAM5 (Source: CESM userguide).

Band Index	Band Min (μm)	Band Max (μm)	Band Min (cm^{-1})	Band Max (cm^{-1})
1	28.57	1000.0	10	350
2	20.00	28.57	350	500
3	15.87	20.00	500	630
4	14.29	15.87	630	700
5	12.20	14.29	700	820
6	10.20	12.20	820	980
7	9.26	10.20	980	1080
8	8.47	9.26	1080	1180
9	7.19	8.47	1180	1390
10	6.76	7.19	1390	1480
11	5.56	6.76	1480	1800
12	4.81	5.56	1800	2080
13	4.44	4.81	2080	2250
14	4.20	4.44	2250	2380
15	3.85	4.20	2380	2600
16	3.08	3.85	2600	3250